

## Electric Double Layer at the Rutile (110) Surface. 2. Adsorption of Ions from Molecular Dynamics and X-ray Experiments

M. Předota,<sup>\*,†,‡</sup> Z. Zhang,<sup>§,||</sup> P. Fenter,<sup>§</sup> D. J. Wesolowski,<sup>⊥</sup> and P. T. Cummings<sup>‡,⊥</sup>

*Institute of Chemical Process Fundamentals, Academy of Sciences of the Czech Republic, 165 02 Prague, Czech Republic, Department of Chemical Engineering, Vanderbilt University, Nashville, Tennessee 37235-1604, Department of Health Physics and Biophysics, Faculty of Health and Social Studies, University of South Bohemia, Jírovčova 24, České Budějovice 370 04, Czech Republic, Argonne National Laboratory, 9700 South Cass Avenue, Argonne, Illinois 60439, Department of Materials Science and Engineering, Northwestern University, Evanston, Illinois 60208-3108, and Aqueous Chemistry and Geochemistry Group, Chemical Sciences Division, Oak Ridge National Laboratory, Oak Ridge, Tennessee 37831-6110*

Received: October 22, 2003; In Final Form: May 3, 2004

Molecular dynamics (MD) simulations were conducted to characterize the microstructure of the interface between aqueous solutions and the (110) surface of rutile ( $\alpha$ -TiO<sub>2</sub>) for hydroxylated and nonhydroxylated surfaces, each either neutral or negatively charged. The fully atomistic description of the rutile surface and its interactions with the fluid phase was based on ab initio calculations, while the aqueous phase was described by the SPC/E model and existing parametrizations for Rb<sup>+</sup>, Na<sup>+</sup>, Sr<sup>2+</sup>, Zn<sup>2+</sup>, Ca<sup>2+</sup>, and Cl<sup>−</sup> ions. Formation of inner-sphere complexes of cations with surface oxygens was identified for all cations studied. On negatively charged surfaces, Zn<sup>2+</sup> is shown to sorb at two bidentate sites, between a bridging and terminal oxygen, and between two terminal oxygens (hydroxylated surface only), while all other cations occupy a tetradentate site, in contact with two terminal and two bridging oxygens in adjacent rows on the crystal surface, and directly above an additional triply coordinated oxygen in the Ti–O surface plane. These differences in inner-sphere binding configuration appear to be related to the bare ionic radii of the cations. Simulation results agree very well with X-ray standing wave and crystal truncation rod studies of the inner-sphere adsorption sites of the cations Rb<sup>+</sup> and Sr<sup>2+</sup>. MD and X-ray results for Zn<sup>2+</sup> adsorption are qualitatively consistent, but important differences in adsorption heights are discussed. Both MD simulations and X-ray studies indicate that, on rutile (110), interaction of Cl<sup>−</sup> with neutral and negatively charged surfaces and with sorbed, multivalent cations is minimal. The hydroxylated surface gives better agreement with experiments than the nonhydroxylated surface and is therefore inferred to be the dominant surface in contact with aqueous solutions at ambient conditions. At the negative, hydroxylated surface, the MD results indicate that Sr<sup>2+</sup> and Ca<sup>2+</sup> also form outer-sphere species that are laterally ordered with respect to the crystal surface structure, though these are much less abundant than the inner-sphere species. At positively charged hydroxylated surfaces, MD simulations indicate Cl<sup>−</sup> adsorption in the tetradentate site 4.3 Å above the surface, with longer-range ordering of ions and water molecules than was observed on neutral or negatively charged surfaces. The adsorption geometries of ions are not sensitive to an increase of temperature to 448 K.

### 1. Introduction

In our previous paper<sup>1</sup> we described the modeling of rutile ( $\alpha$ -TiO<sub>2</sub>) surfaces in contact with aqueous solutions and presented molecular dynamics (MD) simulation results on the structure of water in the interfacial region. In this paper, the same model is applied to study the interaction of dissolved ions with rutile (110) surfaces to determine their preferred adsorption sites, as well as the longer-range water and ion distributions in the interfacial region. We also compare the simulation results with direct experimental observations of rutile (110) single-crystal surfaces in contact with liquid water and electrolyte solutions at ambient conditions, obtained from X-ray standing wave (XSW)<sup>2,3</sup> and X-ray reflectivity [e.g., crystal truncation

rod (CTR)] analysis of near-surface structures.<sup>4,5</sup> The MD results are complementary to the X-ray observations and give more detailed insight into the longer-range interfacial structure and dynamics, including species difficult to image experimentally, such as Cl<sup>−</sup> and hydrogen. Molecular dynamics simulations provide not only the most preferred adsorption positions but also the distribution of ions around these positions, in both axial and lateral directions, which might be taken into account in analysis of experimental data. The goal of this study is to verify the performance of the MD simulation model of the atomistically detailed rutile (110) surface in predicting interfacial phenomena, by comparison with X-ray experiments. On the basis of this comparison, we infer which of the model surfaces is the most realistic. This is a first step to application of the current model to other systems and prediction of properties that are hardly or not at all experimentally measurable. The molecular dynamics simulations thus offer predictive capabilities necessary for deeper understanding of interfacial phenomena.

\* Corresponding author: e-mail predota@icpf.cas.cz.

† Academy of Sciences of the Czech Republic and University of South Bohemia.

‡ Vanderbilt University.

§ Argonne National Laboratory.

|| Northwestern University.

⊥ Oak Ridge National Laboratory.

**TABLE 1: Atomic Charges  $q$ , Lennard-Jones Parameters  $\sigma$  and  $\epsilon$  of SPC/E Water and Ions, Position  $d_{\text{ion-O}}$  of Peak of Ion–Oxygen Pair Correlation Function,<sup>a</sup> and Ion–Water Separation  $d_{\text{ion-W}}$ <sup>b</sup>**

atom	$q$ (e)	$\sigma_{\text{ion}}$ (Å)	$\epsilon_{\text{ion}}$ (kcal/mol)	$\sigma_{\text{ion-O}}$ (Å)	$d_{\text{ion-O}}$ (Å)	$d_{\text{ion-W}}$ (Å)
O	−0.8476	3.166	0.1554	3.166	2.75	
H	+0.4238					
Rb <sup>+</sup>	+1	3.528	0.1	3.348	2.95	2.89
Na <sup>+</sup>	+1	2.583	0.1	2.876	2.47	2.36
Sr <sup>2+</sup>	+2	3.314	0.1	3.240	2.64	2.64
Ca <sup>2+</sup>	+2	2.895	0.1	3.030	2.46	2.42
Zn <sup>2+</sup>	+2	21.34 <sup>c</sup>	$6.329 \times 10^{-14}$ <sup>c</sup>	8.220 <sup>c</sup>	2.06	2.10
Cl <sup>−</sup>	−1	4.401	0.1	3.785	3.23	3.19

<sup>a</sup> This work. <sup>b</sup> From ref 17. <sup>c</sup> Refitted purely repulsive LJ potential for zinc.

## 2. Model and Simulation Method

The molecular dynamics simulations of TiO<sub>2</sub>–water interfaces were performed in a slab geometry in aqueous solutions sandwiched between two parallel TiO<sub>2</sub> (110) walls (see Figure 3 of ref 1). Therefore, the system has two identical solid–fluid interfaces and the reported properties are averages over both interfaces. The comparison of results at each of the interfaces serves also as a verification of convergence of the simulations. The intervening slab of water and dissolved ions is thick enough to achieve bulk behavior in the central region, which shows little or no influence of the crystal surfaces and which retains the correct water density for the conditions of 298 K and 1 atm. The whole system is periodically replicated in the lateral  $x$  and  $y$  directions parallel to the surface plane. As described in ref 1, the rutile (110) surface is characterized by a plane of Ti atoms, including rows of exposed, five-coordinated Ti atoms (terminal Ti atoms) and rows of doubly coordinated bridging oxygens (BO) that protrude above the surface plane and are bound to two six-coordinated Ti atoms in the surface plane. The surface plane also includes rows of exposed, triply coordinated oxygens, designated O(s). The exposed terminal Ti atoms are always covered by either a strongly associated water molecule (referred to as the terminal water) or a bonded hydroxyl group (referred to as the terminal hydroxyl). In our simulations, the Ti–O and O–H bond lengths of the bridging and terminal hydroxyls (Ti–O bond only for unprotonated bridging oxygen) are fixed at their ab initio values,<sup>6,7</sup> but the bonds are permitted to rotate. All atoms on and below the surface Ti–O plane are relaxed to their ab initio configuration but are held rigid in the simulations. We chose to keep the bulk of the crystal slabs rigid because we feel that the ab initio configuration may be more accurate, and considerable computational time is saved by fixing the positions of all but the bridging and terminal species.

For the solvent we used the rigid, nonpolarizable SPC/E water model<sup>8</sup> because of its simplicity and the availability of ion–water potentials specifically parametrized for SPC/E water.<sup>9,10</sup> Furthermore, as discussed in ref 1, this model reproduces the phase envelope, density, structure, and dielectric properties of water and aqueous electrolyte solutions remarkably well over wide ranges of temperature, density, and composition,<sup>11–13</sup> even though the SPC/E model was parametrized by fitting only the density and configurational energy of liquid water at 300 K and 1 atm.<sup>8</sup> The partial charges and Lennard-Jones (LJ) potential parameters of SPC/E water and the ions (Na<sup>+</sup>, Rb<sup>+</sup>, Ca<sup>2+</sup>, Sr<sup>2+</sup>, Zn<sup>2+</sup>, and Cl<sup>−</sup>) are given in Table 1. The Lorentz–Berthelot combining rules<sup>14</sup> are used for the cross interactions, i.e.,  $\sigma_{ij} = (\sigma_i + \sigma_j)/2$ ,  $\epsilon_{ij} = \sqrt{\epsilon_i \epsilon_j}$ . For zinc we used the same potential as given in ref 15, i.e., purely repulsive potential, which was given in the form  $U_{ij} = A_{ij}/r_{ij}^{12}$  with combining rule  $A_{ij} = A_i' A_j'$  and

$A_{\text{Zn}'} = 0.9716 \times 10^{-4} \text{ kJ}^{1/2} \text{ mol}^{-1/2} \text{ nm}^6$ . To be able to combine this potential with LJ potentials of other ions, we have refitted the original zinc potential to a LJ form with a negligible attractive part. This is achieved by choosing very small potential depth  $\epsilon$  of the refitted potential; the parameter  $\sigma$  is then given by a condition that the product  $4\epsilon\sigma^{12}$  equals the coefficient  $A$  of the original potential. In accord with the combining rule given in ref 15, we have used the geometric mean for both  $\sigma_{ij}$  and  $\epsilon_{ij}$  when zinc ion was involved.

The planar structure of the rutile (110) surface was obtained from ab initio calculations on a five-layer slab exposed to a water monolayer on both surfaces by use of periodic density functional theory.<sup>1,6,7</sup> Four different surfaces were studied: the hydroxylated and nonhydroxylated surfaces, each either neutral or negatively charged with surface charge density  $-0.208 \text{ C/m}^2$ . Details of the construction and modeling of these surfaces and all details concerning molecular dynamics simulations of the two parallel rutile surfaces with aqueous solutions between them are given in ref 1. In all cases, the total number of ions, associated SPC/E water molecules, and dissociated water molecules (terminal hydroxyls) summed to 2048. The total charge of the system, comprising the solution and surface, was zero. In the case of the negatively charged surfaces, the electroneutrality of the entire system is achieved by a surplus of positive ions in the solution. For the size of our simulation cells, a surface charge density of  $-0.208 \text{ C/m}^2$  results in surface charge  $-36e$ , which is balanced by a proportional excess of cations. At the start of the simulations, the ions are placed randomly in the solution.

The equilibration runs were at least 0.3 ns with a time step of 1.2 fs. Production runs were about 1–2 ns with a time step of 1.0–1.2 fs. The long simulation runs were dictated primarily by the time needed to obtain good statistics of lateral and axial density profiles of ions. The time evolution of separate contributions to the total energy (e.g., electrostatic and nonelectrostatic interactions between ions and water molecules, wall–water and wall–ion contributions), the total pressure and other properties were monitored to verify the convergence of results. The final axial density profiles (i.e., along the surface normal) of ions were compared against intermediate results from  $1/3$  of the production run length to verify that the system was well equilibrated. In a few cases where satisfactory equilibration of the system prior to production run was in question, the final configuration served as initial configuration for a new production run and the simulation was restarted.

## 3. Results

We have performed simulations at  $T = 298.15 \text{ K}$  and  $\rho_{\text{bulk}} = 1 \text{ g/cm}^3$  and at  $T = 448 \text{ K}$  and  $\rho_{\text{bulk}} = 0.9 \text{ g/cm}^3$  (the latter being the density of vapor-saturated liquid water at 448 K). The averaged configurations of ions, water molecules, and surface oxygens at the higher temperature were found to be quite similar to their configurations at room temperature, and therefore we report here only the results at room temperature. Diffusivities and oscillations about equilibrium positions are, however, greater at the higher temperature. The results at negatively charged surfaces with surface charge density  $-0.208 \text{ C/m}^2$  are compared with results at neutral surfaces, i.e., surfaces bearing zero net charge but nonzero partial charges on all atoms.<sup>1</sup> We have also run some simulations at surface charge density  $-0.104 \text{ C/m}^2$  to see the effect of changing surface charge density on the overall water/ion distributions. While reducing surface charge density by a factor of 2 results in a proportionally smaller number of adsorbed ions, the surface adsorption positions change

**TABLE 2: Number of Ions Used in Simulations of Neutral Surfaces and Negative Surfaces<sup>a</sup> with Surface Charge Density  $\sigma_H = -0.208 \text{ C/m}^2$** 

cation	neutral		negative	
	no. of cations	no. of $\text{Cl}^-$	no. of cations	no. of $\text{Cl}^-$
monovalent $\text{Rb}^+$ , $\text{Na}^+$	12	12	48	12
divalent $\text{Sr}^{2+}$ , $\text{Ca}^{2+}$ , $\text{Zn}^{2+}$	16	32	27	18

<sup>a</sup> In this case there is a net total charge of  $-36e$  on the two surfaces, which is balanced by a surplus of cations in the solution, which makes the simulation cell neutral.

by less than  $0.05 \text{ \AA}$ , and no gross changes in longer-range structure are indicated. This is consistent with our atomistic modeling of the surface, where surface charge density determines the number of charged surface sites (and consequently the number of adsorbed ions), but the local structure of each of these sites is independent of the surface charge density. Therefore, the results presented here for  $\sigma_H = -0.208 \text{ C/m}^2$  are representative for an important range of negative surface charge densities (i.e., pHs of 5.5–10 at room temperature) exhibited by real rutile in aqueous solutions. Undoubtedly, at real solution/solid interfaces, the change in the charge density of the fixed plane of charge represented by the surface will influence the distribution of ions in the diffuse portion of the electrical double layer. Such ions are apparently not ordered with respect to the crystal surface structure and therefore were not directly imaged by our current X-ray methods. Our simulations at present do not give a clear indication of a well-developed diffuse layer, and this may be an artifact of the boundary conditions of the simulations and the statistics associated with the few ions that are not specifically adsorbed at the surface. However, this study shows that the binding geometries of ions and water molecules in contact with the surface oxygens are not significantly influenced by the overall charge density of the surface.

The positions of the peaks in the species density profiles normal to the (110) surface plane were identical for both interfaces (left and right) in all simulation runs. In some cases, the heights of the peaks of ionic density profiles differed at each of the interfaces, because of different densities of ions at the two surfaces, as a result of equilibration from the initial random configuration. While the equilibration time was long enough to allow the ions to drift from the initial configuration toward the surface, the simulation time is definitely not long enough to allow the exchange of ions between the two surfaces. The number of ions used in our simulations is given in Table 2.

As will be confirmed, oxygen–cation interactions play the major role in determining the structure of adsorbed cations, and the radius of ions is the key information for the discussion of adsorption of various cations. The most probable separation of the center of an ion from the centers of oxygens of surrounding water molecules in bulk water,  $d_{\text{ion-O}}$ , is directly available from the location of the first peak of the ion–oxygen pair correlation function (PCF)  $g_{\text{ion-O}}$ , which is plotted in Figure 1 for all ions; the separations  $d_{\text{ion-O}}$  are given in Table 1. The pair correlation functions shown in Figure 1 were obtained from simulations of ions in aqueous solution between neutral rutile surfaces, when the ions are fully solvated by water molecules and their interaction with the surfaces is weak. For ions adsorbed on charged surfaces, the distances ion–oxygen of a water molecule remain the same, but at larger separations the pair correlation function  $g_{\text{ion-O}}$  falls below unity due to lack of water molecules in the half-space around adsorbed ions, which is occupied by

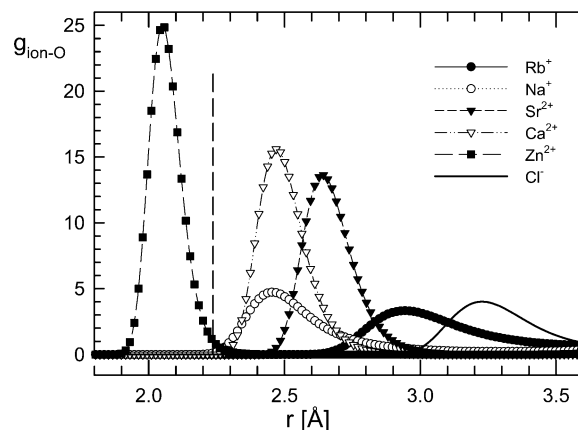


**Figure 1.** Ion–oxygen (of associated water molecule) pair correlation functions from MD simulations. These functions are insensitive to the particular choice of surface. The positions of the peaks  $d_{\text{ion-O}}$  are given in Table 1. The dashed vertical line at  $2.23 \text{ \AA}$  indicates the minimum ion–O separation necessary for forming simultaneously four bonds in tetradentate site.

the rutile surface. In the last column of Table 1 we also include the average values of ion–water separations  $d_{\text{ion-W}}$  based on a review<sup>17</sup> of numerous works on ionic aqueous solutions, incorporating X-ray and neutron diffraction values as well as simulation data. As can be seen, the model used in this study is consistent with these values, with the largest deviation for  $\text{Na}^+$  ( $0.11 \text{ \AA}$ ) and  $0.0$ – $0.06 \text{ \AA}$  for all other ions.

**A. Adsorption of  $\text{Rb}^+$ .** The axial density profile of rubidium, defined as the number density of ions (i.e., the number of ions per cubic angstrom), is given in Figure 2a. This plot, in contrast to axial density profiles normalized by the uniform distribution of ions, has two advantages, namely, (i) the volume of the slab and consequently the average density are not uniquely defined, while the number density is well-defined; and (ii) the number of ions at the interfacial layer for a charged surface should depend on the surface charge rather than on the total number of ions. Thus, the first peak of the  $\text{Rb}^+$  axial density profile is not sensitive to the total number of ions present in the solution, as confirmed by simulations with different numbers of ions. The zero point of the horizontal axis in Figure 2a and in all other axial profiles was defined as the plane bisecting the centers of surface Ti and O(s) atoms on the rutile (110) surface if the surface was not relaxed but had the ideal bulk crystalline structure. This reference frame, which is easily projected from the position of our third and fourth slab layers, which keep their ideal crystal structure, was also used in ref 1; the deviations of the (110) surface atoms in contact with bulk water from their positions in the unrelaxed bulk crystal termination, are on the order of  $\pm 0.1 \text{ \AA}$ . This choice of reference frame is important as it is the same as that used in X-ray experiments,<sup>18,19</sup> which enables direct comparison of X-ray and MD ionic heights.

The axial density profile of  $\text{Rb}^+$  for all surfaces studied (Figure 2a) reveals strong adsorption of  $\text{Rb}^+$  at negatively charged surfaces with a peak at  $3.55 \text{ \AA}$  for the negative hydroxylated surface and  $3.5 \text{ \AA}$  with a shoulder at  $3.9 \text{ \AA}$  for the negative nonhydroxylated surface. Rubidium also adsorbs, in a smaller amount, on the neutral hydroxylated surface at  $3.8 \text{ \AA}$  from the surface.  $\text{Rb}^+$  does not adsorb on the neutral nonhydroxylated surface; the tiny peak around  $4 \text{ \AA}$  on the inset axial profile covers less than one ion on the total rutile surface, and this ion is not laterally ordered.

The lateral distribution of adsorbed  $\text{Rb}^+$  in a layer around the first peak of axial density gives information on the adsorption site relative to surface atoms. From the 3D plot of the density



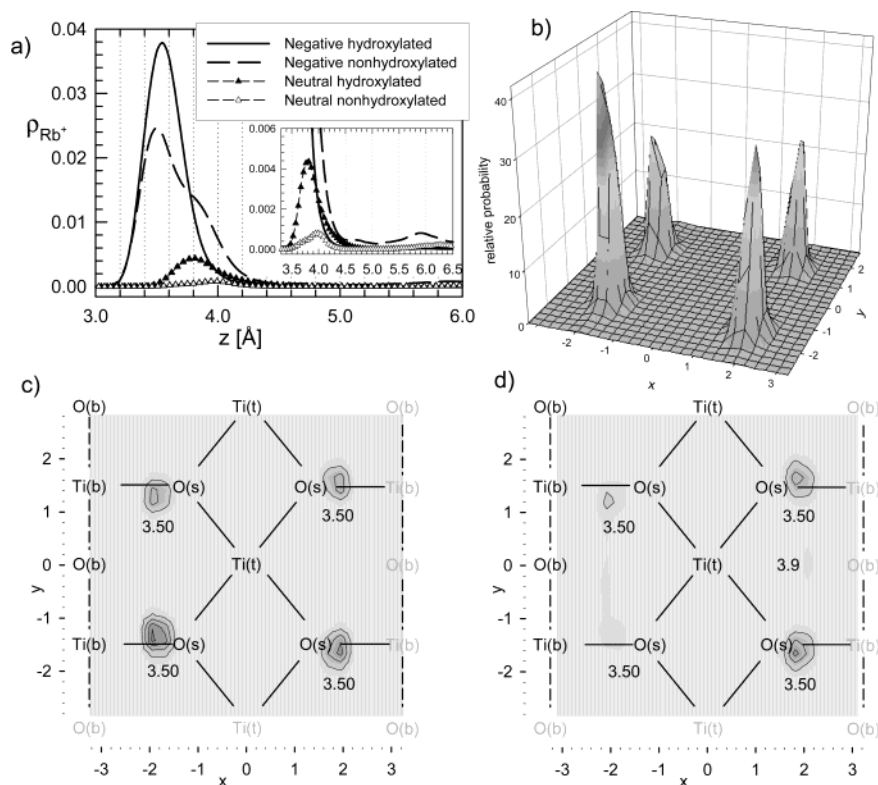


**Figure 2.** Axial profiles for all surfaces (a) and lateral profiles (b–d) of adsorbed  $\text{Rb}^+$  on negative surfaces. The contour plot (c) is a projection of the 3D plot (b) of density of ions above the negative hydroxylated surface and both capture the strong adsorption peak at tetradentate site. In addition, at negative nonhydroxylated surface (d) a small peak at bidentate site between bridging and terminal oxygens, corresponding to the shoulder of corresponding axial density profile at 3.9 Å, is observed. The positions of the last  $\text{TiO}_2$  layer atoms, and of the bridging off-plane atoms, are indicated as follows: Ti(t), terminal Ti; Ti(b), bridging Ti; O(s), surface in-plane O; O(b), bridging O; the Ti–O bonds in the surface plane are indicated by solid lines; the off-plane bonds to the bridging oxygen are indicated by dashed lines. Each peak of increased density on lateral profiles is labeled by its height above the surface.

of  $\text{Rb}^+$  in the selected layer as a function of lateral  $x$  and  $y$  coordinates (Figure 2b), we construct contour plots (Figure 2c,d) with darker areas denoting areas of higher ionic concentration. The contours are shown in linear increments of 10, where unit density corresponds to homogeneous distribution of ions along the surface.

In all cases of inner-sphere adsorption,  $\text{Rb}^+$  adsorbs at a tetradentate site forming four bonds with oxygens of the surface, namely, two bridging and two terminal oxygens,<sup>1</sup> which are shown in the snapshot of adsorbed  $\text{Rb}^+$  (Figure 3) as the closest oxygen atoms to  $\text{Rb}^+$ . In the case of the charged nonhydroxylated surface, there is only one terminal hydroxyl group available for bonding with the adsorbed  $\text{Rb}^+$  (see Figure 2 of ref 1) but the oxygen of the corresponding, chemisorbed water molecule occupying the adjacent terminal site (only slightly higher above the surface, as recognized in ref 1) forms the fourth member of the tetradentate surface site. The tetradentate site lies almost directly above a triply coordinated surface oxygen O(s) lying in the Ti–O surface plane; the presence of this oxygen might further assist in making the tetradentate site very favorable for cation adsorption. The hydrogens of terminal hydroxyls and bridging hydroxyls (if present) minimize the  $\text{Rb}^+$ –H repulsion by moving away from the  $\text{Rb}^+$  ion; see Figure 3. We believe that it is the  $\text{Rb}^+$ –H repulsion which prevents inner-sphere  $\text{Rb}^+$  adsorption on the neutral nonhydroxylated surface, because in this case both oxygens above terminal Ti atoms belong to water molecules, i.e., have two hydrogens each, which makes it hard (or impossible) for them to orient without introducing  $\text{Rb}^+$ –H or H–H repulsion.  $\text{Rb}^+$  adsorbs as an inner-sphere adsorbate and is partially desolvated, since the terminal and bridging

oxygens substitute water molecules in the first hydration shell of the cation.

The shoulder on the axial  $\text{Rb}^+$  profile at the negative nonhydroxylated surface at 3.9 Å is formed by bidentate  $\text{Rb}^+$  ions, which make bonds with one bridging oxygen and one terminal oxygen. This site is much less populated than the tetradentate site as is clear from the small shoulder of the axial profile and small density of  $\text{Rb}^+$  at this site in Figure 2d.

The tetradentate site geometry of  $\text{Rb}^+$  adsorption observed in MD is in excellent agreement with the results of a recent in situ X-ray CTR study of rutile (110) single-crystal surfaces submerged in 1 mol·kg<sup>−1</sup>  $\text{RbCl}$  solutions (pH 12) conducted at the Advanced Photon Source, Argonne National Laboratory.<sup>18,20</sup> These experiments indicate a tetradentate adsorption site at a height of  $3.44 \pm 0.03$  Å above the unrelaxed surface (CTR measurements also confirm surface relaxation of ca.  $\pm 0.1$  Å), and the lateral position of sorbed  $\text{Rb}^+$  relative to the (110) surface atom positions is essentially the same as that predicted by MD; see Table 3. The CTR measurements do not indicate a subordinate, bidentate sorption site for  $\text{Rb}^+$ , suggesting that the hydroxylated surface in our simulations better approximates the behavior of the real solution and solid.

**B. Adsorption of  $\text{Na}^+$ .** In terms of potential parameters, the only difference between  $\text{Rb}^+$  and  $\text{Na}^+$  is the smaller Lennard-Jones  $\sigma_{\text{ion}}$  parameter of  $\text{Na}^+$ , which results in the minimum of  $\text{Na}^+$ –O potential at about 2.2 Å and the peak  $\text{Na}^+$ –O PCF occurring at 2.47 Å (Figure 1). As a result,  $\text{Na}^+$  adsorbs significantly closer to the surface than  $\text{Rb}^+$ . The tetradentate site adsorption height is 2.9 Å for negative surfaces and 3.15 Å for the neutral hydroxylated surface (Figure 4a). Unlike  $\text{Rb}^+$ ,

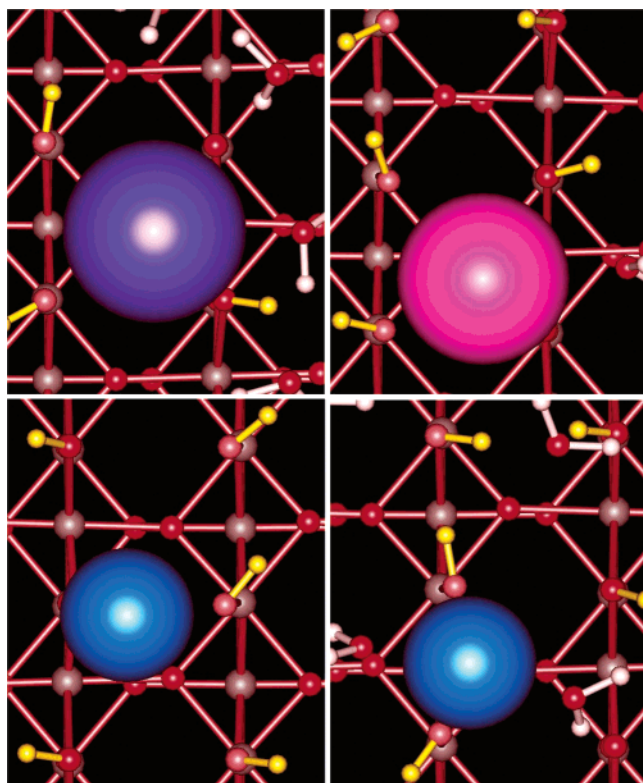


**Figure 3.** Snapshots of the negative hydroxylated surface (looking perpendicularly toward the surface) with adsorbed  $\text{Rb}^+$  (top left) and  $\text{Sr}^{2+}$  (top right) at tetradentate sites,  $\text{Zn}^{2+}$  bidentate between BO and TO (bottom left), and  $\text{Zn}^{2+}$  bidentate between two terminal oxygens (bottom right). Oxygens are red with terminal oxygens shown in a lighter hue, hydrogens of water molecules are white, hydrogens of surface hydroxyls are yellow, and titanium is gray. Only adsorbed ions are shown in actual size; other atoms are scaled down for clarity. Water molecules further from the surface than the ion are not shown.

for which only a small fraction adsorbs at the bidentate site on the negative nonhydroxylated surface,  $\text{Na}^+$  adsorbs on this surface in equal amounts in the tetradentate and bidentate sites, the latter at a height of 3.42 Å. As in the case of  $\text{Rb}^+$ , no significant adsorption of  $\text{Na}^+$  on the neutral nonhydroxylated surface is observed. No X-ray results on the structure of  $\text{Na}^+$  at the interface are available because of the greater technical difficulty of observing low- $Z$  elements in situ at the solid–liquid interface, including the significant adsorption of characteristic X-ray fluorescence signals by the micrometer-thick solution (for X-ray standing wave measurements), and the small differences in electron density between  $\text{Na}^+$  and  $\text{H}_2\text{O}$  (for X-ray reflectivity measurements).

**C. Adsorption of  $\text{Sr}^{2+}$ .** The charge of  $+2e$  of the  $\text{Sr}^{2+}$  ion and its smaller radius than  $\text{Rb}^+$  (Table 1) results in a stronger tendency of  $\text{Sr}^{2+}$  to retain its hydration shell and to stay fully solvated than is the case for monovalent ions.  $\text{Sr}^{2+}$  moves together with its hydration shell, a situation that makes its dynamics slower than that of  $\text{Rb}^+$ . The rough estimates of  $\text{Rb}^+$  and  $\text{Sr}^{2+}$  diffusivities in water from our simulations are about  $2.3 \times 10^{-5}$  and  $1.3 \times 10^{-5}$   $\text{cm}^2/\text{s}$ , respectively, in fair agreement with experimental values of  $2.06 \times 10^{-5}$  and  $0.8 \times 10^{-5}$   $\text{cm}^2/\text{s}$ ,<sup>21</sup> considering our MD data were obtained from the bulk region in the middle of the slab, where only a few dozen ions are present. Because of their lower diffusivity, the simulation time span needed to sample adequately a system with divalent ions was usually longer than that for monovalent ions. The axial density profile of  $\text{Sr}^{2+}$  (Figure 4d) features an adsorption peak at 3.2 Å at both negative surfaces. This peak is identified as a

tetradentate site from the lateral profiles of  $\text{Sr}^{2+}$  (Figures 4e,f and 3). In addition, bidentate site adsorption takes place on the negative nonhydroxylated surface at height 3.65 Å. There is very good agreement between the height of the tetradentate site predicted by MD and the height determined from synchrotron XSW measurements,<sup>18,19</sup> which is  $3.07 \pm 0.07$  Å (Table 3). The bidentate site, however, is not observed in the XSW study, reinforcing the suggestion, based on the  $\text{Rb}^+$  CTR studies, that the hydroxylated simulation surfaces better describe the interaction of real rutile (110) with real aqueous solutions.

The MD simulations predict that a small fraction of  $\text{Sr}^{2+}$  ions, about 10%, remain solvated and adsorb as an outer-sphere species above the negative surfaces at 5.5–6.3 Å. The lateral profile of these ions is well-defined, with preferred positions above bridging Ti atoms at the nonhydroxylated surface and above terminal Ti atoms at the hydroxylated surface, though it is not visible in Figure 4e,f due to the large probability scale set by the density peaks at shorter distances. The preferred lateral position at this layer results from a rather complex interplay of water molecule interactions between the surface and  $\text{Sr}^{2+}$  ions. The latter site is not directly observed in the X-ray standing wave measurements, but these experimental results are not necessarily inconsistent with the MD simulations due to the relatively small fraction of ions that are adsorbed at the outer-sphere species. Additional measurements will be necessary to experimentally test this possibility.

At neutral surfaces,  $\text{Sr}^{2+}$  ions never adsorb on the surface directly and remain fully solvated with a first peak of the axial density profile of  $\text{Sr}^{2+}$  at heights 5.5–6.0 Å above the surface. This peak covers only 2–3 ions at each surface and the peak density is only about 6 times the homogeneous density of ions in the bulk. The lateral distribution of these atoms is rather flat, with increased density above bridging Ti atoms. This observation is in accord with experimental pH titration data,<sup>18</sup> which show that  $\text{Sr}^{2+}$  adsorption on rutile powders with the (110) surface as the predominant exposed face is negligible at pHs near the point of zero charge ( $\text{pH}_{\text{pzc}} = 5.4 \pm 0.2$  at 298 K<sup>22</sup>).

**D. Adsorption of  $\text{Ca}^{2+}$ .** The relation of  $\text{Ca}^{2+}$  to  $\text{Sr}^{2+}$  is similar to that of  $\text{Na}^+$  to  $\text{Rb}^+$ .  $\text{Ca}^{2+}$  is smaller than  $\text{Sr}^{2+}$  and therefore adsorbs closer to the surface; the tetradentate site is at a height of 3.0 Å at both negative surfaces and the bidentate site is 3.47 Å high at the negative nonhydroxylated surface (Figure 5a–c). As for the monovalent ions, the probability of adsorption at the bidentate site is greater for the smaller ion ( $\text{Ca}^{2+}$  in this case) than for the larger ion, resulting in bidentate adsorption of  $\text{Ca}^{2+}$  predominating at the negative nonhydroxylated surface and formation of a small bump on the axial profile of  $\text{Ca}^{2+}$  at negative hydroxylated surface, which indicates minority adsorption at the bidentate site.

As for  $\text{Sr}^{2+}$ ,  $\text{Ca}^{2+}$  does not adsorb on neutral surfaces directly, but a small amount adsorbs at 5.7 Å above the neutral nonhydroxylated surface and at two positions, 5.3 and 6.0 Å, on the neutral hydroxylated surface. These positions and amounts of adsorbed ions at neutral surfaces are similar to those of adsorbed solvated  $\text{Ca}^{2+}$  ions at negative surfaces (see inset of Figure 5a) but the number of adsorbed solvated ions is in both cases about 10% (i.e., two ions per surface) of the number of partially desolvated ions adsorbing at negative surfaces at distances below 4 Å. Experimental X-ray data for  $\text{Ca}^{2+}$  adsorption at rutile surfaces are not available due to similar arguments as discussed above for  $\text{Na}^+$ .

**E. Adsorption of  $\text{Zn}^{2+}$ .** Zinc is the by far the smallest of all the ions studied, with the first peak in the  $\text{Zn}^{2+}$ –O pair correlation function at 2.06 Å (Figure 1). Its axial and lateral

**TABLE 3: Tetradentate (TD) and Bidentate (BD) Adsorption Sites of Ions<sup>a</sup>**

ion	type <sup>b</sup>	adsorption site					
		MD		X-ray <sup>18</sup>		geom estimate	
		height <i>z</i> (Å)	<i>x</i> (Å)	<i>z</i> (Å)	<i>x</i> (Å)	<i>z</i> (Å)	<i>x</i> (Å)
Rb <sup>+</sup>	TD	3.5	1.9	3.44 ± 0.03	1.93 ± 0.05	3.55	2.09
Rb <sup>+</sup>	BD-BOTO	3.9 <sup>c</sup>	2.2 <sup>c</sup>	<i>d</i>	<i>d</i>	3.95	2.20
Na <sup>+</sup>	TD	2.9	1.8	<i>e</i>	<i>e</i>	2.70	1.88
Na <sup>+</sup>	BD-BOTO	3.4 <sup>c</sup>	2.1	<i>e</i>	<i>e</i>	3.35	2.05
Sr <sup>2+</sup>	TD	3.2	1.9	3.07 ± 0.07	1.97 ± 0.12	3.04	1.95
Sr <sup>2+</sup>	BD-BOTO	3.7 <sup>c</sup>	2.2	<i>d</i>	<i>d</i>	3.59	2.10
Ca <sup>2+</sup>	TD	3.0	1.9	<i>e</i>	<i>e</i>	2.68	1.87
Ca <sup>2+</sup>	BD-BOTO	3.5 <sup>c</sup>	2.2 <sup>c</sup>	<i>e</i>	<i>e</i>	3.35	2.05
Zn <sup>2+</sup>	TD	<i>d</i>	<i>d</i>	<i>d</i>	<i>d</i>		
Zn <sup>2+</sup>	BD-BOTO	2.85 <sup>f</sup> , 3.05 <sup>c</sup>	2.2	3.12 ± 0.14	2.55 ± 0.06 <sup>g</sup>	2.77	1.91
Zn <sup>2+</sup>	BD-TOTO	3.45 <sup>f</sup>	0	2.6 ± 0.25	0.4 ± 0.45	3.42	0

<sup>a</sup> As observed in MD simulations and X-ray experiments, and as predicted from simple geometric estimates of these sites based on the geometry of rutile surface and size of ions, quantified by  $d_{\text{ion-O}}$ . <sup>b</sup> The bidentate site between bridging and terminal oxygens is given for all ions; for zinc, the bidentate site between two terminal oxygens is given in addition. <sup>c</sup> Site observed only at negative nonhydroxylated surface. <sup>d</sup> Site not observed by X-ray or MD. <sup>e</sup> Experimental data not available. <sup>f</sup> Site observed only at negative hydroxylated surface. <sup>g</sup> Site identified as monodentate adsorption to BO by X-ray standing wave measurements.

profiles (Figure 5d–f) distinguish Zn<sup>2+</sup> from all other cations studied. First, the tetradentate adsorption site observed for all other cations is completely missing. Instead, for both negative surfaces, Zn<sup>2+</sup> adsorbs in a bidentate site between bridging and terminal oxygens at heights of 2.85 Å for hydroxylated and 3.05 Å for nonhydroxylated surfaces. This site, shown in the bottom left panel of Figure 3, is the same type of bidentate site observed for Na<sup>+</sup>, Sr<sup>2+</sup>, and Ca<sup>2+</sup> at negative nonhydroxylated surfaces. At the negative hydroxylated surface, Zn<sup>2+</sup> adsorbs also at another site at a height of 3.45 Å, which is a bidentate site between two terminal oxygens. This site, shown in the bottom right panel of Figure 3, is not observed for other ions or surfaces studied. It is the small size of Zn<sup>2+</sup> that enables it to fit between two terminal oxygens. However, Zn<sup>2+</sup> is at the same time 1.45 Å higher than the terminal oxygens, which are 2.0 Å from the surface.

Synchrotron XSW determination of Zn<sup>2+</sup> adsorption on rutile (110)<sup>18,19</sup> indicates that there are two distinct adsorption sites: a monodentate site bound to a bridging oxygen and a subordinate bidentate site between terminal oxygens. In this respect, the XSW measurements agree better with the MD results for the negatively charged hydroxylated surface. However, in each case the ion site is laterally displaced in a direction perpendicular to the oxygen rows from the nominal high-symmetry site. The experimentally observed monodentate site for Zn, while qualitatively similar to the MD-derived site bridging between BO and TO sites (note that this bidentate site in Figure 3 is displaced by less than 1 Å from the ideal position of monodentate site above BO), is distinct in that the experimentally observed distance between Zn and the terminal oxygen is substantially larger than a Zn–O bond length. Calculated Zn–O distances from X-ray data assuming unrelaxed surface oxygen locations are 2.0 and 2.8 Å to the BO and TO, respectively.<sup>18,19</sup> While the former is consistent with the optimal Zn–O bond length derived by MD simulations, the latter is too large to accommodate a Zn–O bond.

The overall similarity in the two distinct adsorption sites, as derived independently by MD and X-ray measurements, further supports the notion that the negatively charged hydroxylated surface represents the actual surface configuration. However, additional quantitative discrepancies are observed in MD- and X-ray-derived ion heights for the two sites. XSW measurements reveal that the ion heights above the Ti–O surface plane are 3.12 ± 0.14 Å for the monodentate site bound to the bridging oxygen and 2.60 ± 0.25 Å for the bidentate site between two

terminal oxygens; that is, the experiment predicts the bidentate site between two terminal oxygens to be closer to the surface than the other site. The experimentally derived height of the bidentate Zn<sup>2+</sup> between two terminal oxygens of 2.6 Å is only 0.6 Å higher than the terminal oxygens themselves. Assuming that the terminal oxygens are found in their respective bulklike locations, this leads to terminal oxygen–zinc distance of 1.6 Å ( $1.6^2 = 0.6^2 + 1.48^2$ , where 1.48 Å is half of the lattice spacing 2.96 Å giving separation of adjacent terminal oxygens), which is significantly less than the preferred Zn–O distance (see Figure 1). Below are a few possibilities for resolving this discrepancy:

(1) The experimentally observed bidentate species is only a minor (~25%) component of the adsorbed Zn, and as such the derived uncertainty in the Zn height is relatively large (~0.3 Å) even when only statistical error is considered. Furthermore, as a minority species its derived location may be sensitive to any systematic errors that may be present in the XSW data, which are not reflected in stated uncertainties.

(2) Assuming an ideal Zn–O distance of 2.06 Å and the X-ray measured height of 2.6 Å, the terminal oxygens would need to displace laterally by ~1 Å perpendicular to the oxygen rows to comply with these distances. MD simulations observe minimal tilting of the TO bond, even in the presence of zinc. Even though the overall agreement of our model with experimental data for both pure water and all other ions provides solid justification of the model, one cannot rule out the possibility that the close approach of Zn<sup>2+</sup> to the surface may induce additional effects (change of partial surface charges, modification of surface structure) that were not taken into account in parametrization of the model.

(3) It is possible that chemical effects not included in the present MD simulations may be significant in the case of Zn–rutile interactions. For instance, a possibility which is not considered by MD simulations is that zinc adsorbs as Zn(OH)<sup>+</sup>. This possibility has been suggested on the basis of the application of surface complexation models to explain pH titration and proton release measurements of rutile powders where the Zn height and adsorption sites were constrained by XSW results.<sup>18,19</sup> This possibility is further supported by the observation that hydrolysis was not needed to explain the titration data of any other ion that was studied (including Na<sup>+</sup>, Rb<sup>+</sup>, Ca<sup>2+</sup>, and Sr<sup>2+</sup>),<sup>18</sup> and for Rb<sup>+</sup> and Sr<sup>2+</sup> there is nearly quantitative agreement between the MD- and X-ray-derived ion positions where X-ray data are available. However, incorporation



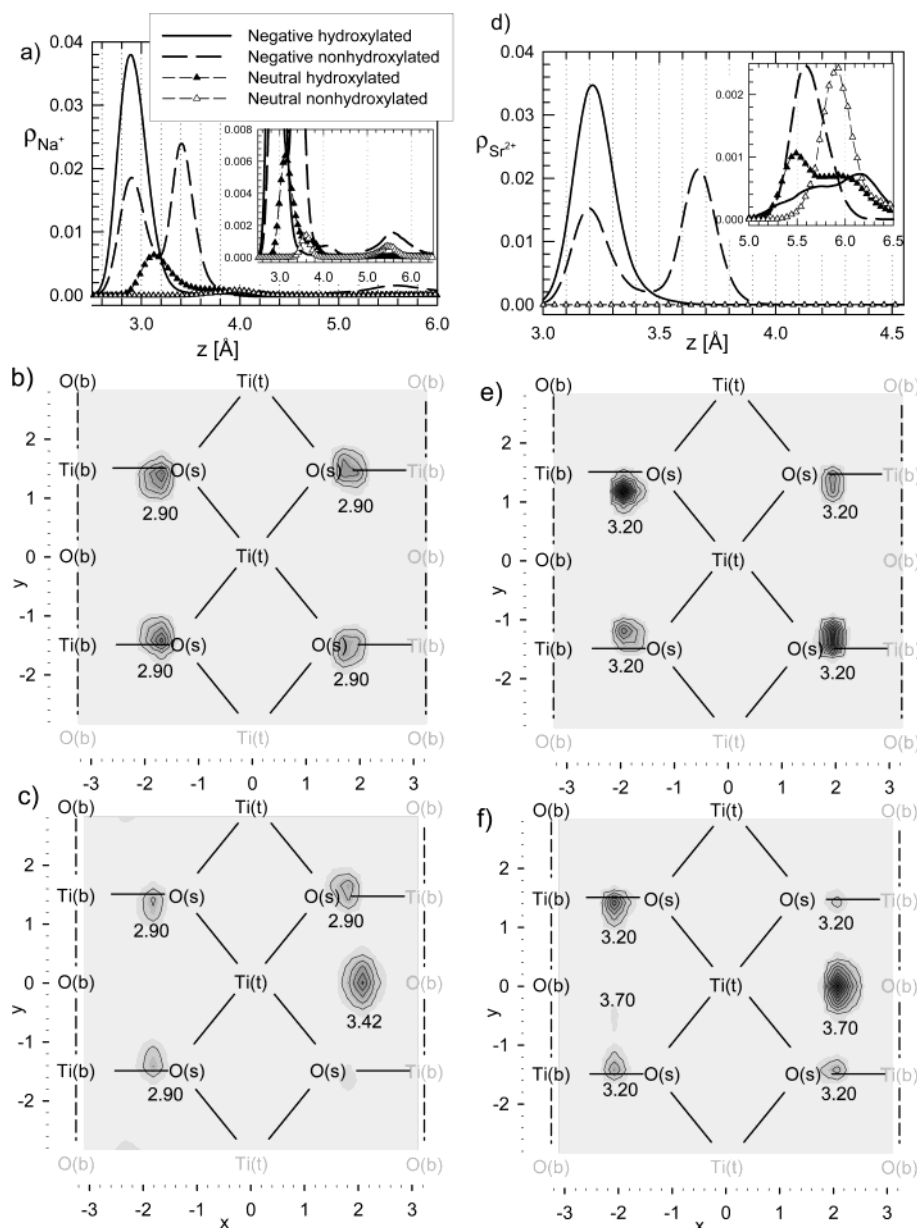


**Figure 4.** Adsorption of  $\text{Na}^+$  (left column) and  $\text{Sr}^{2+}$  (right column). Axial profiles for all surfaces (a, d) and lateral profiles at negative hydroxylated (b, e) and negative nonhydroxylated (c, f) surfaces are shown.

of  $\text{Zn}(\text{OH})^+$  into the MD simulations is not practical at this time, due to the lack of ab initio data on the interaction potentials of this species with water molecules or interaction potentials with SPC/E water molecules. Such changes in the Zn speciation might be expected to have a substantial impact on the local Zn(II) coordination geometry (e.g., Zn–O bond length and coordination number). For instance, the Zn–O bond distance is expected to change by  $\sim 0.3$  Å upon changing the oxygen coordination number from 4 to 6. Such changes, coupled with the relatively large error in the experimentally derived height of the bidentate Zn species, may help to explain the discrepancy between the MD and X-ray derived ion positions. Furthermore, changes in the structure of the Zn–O coordination shell could conceivably drive lateral displacements of the terminal oxygens that are needed to explain the XSW-derived Zn height and that are not observed in the present MD simulations.

**F. Adsorption of  $\text{Cl}^-$ .** Because of the termination of the rutile surface by oxygens, cations are naturally attracted to the surface, but anions are naturally repelled, even at neutral surfaces. At net negatively charged surfaces, anions are even more strongly

repelled. Nevertheless, it has been postulated that when multivalent cations adsorb on mineral surfaces, there may be coadsorption of background electrolyte anions.<sup>24</sup> Therefore, we examined our simulation results for evidence of such coadsorption, even though XSW studies of  $\text{Sr}^{2+}$  and  $\text{Zn}^{2+}$  adsorption on rutile (110) did not reveal any effect of the background electrolyte concentration on cation sorption geometry, in experiments extending over several orders of magnitude in background electrolyte concentration.<sup>18,23</sup>

Whereas the number of adsorbed cations at the negative surfaces is about 36 and 18 for the monovalent and divalent cations, respectively, the number of anions at distances smaller than 7.5 Å observed in the simulations is typically 1–2 ions, which enhances statistical noise and limits sampling of our molecular dynamics data on  $\text{Cl}^-$  structure. We therefore present only selected data on  $\text{Cl}^-$  structure to document our findings. No X-ray experimental data on the position of  $\text{Cl}^-$  at the interface are available due to the low energy of the characteristic X-ray fluorescence line, which is too strongly absorbed in water to be seen; for X-ray reflectivity, its low atomic number (and

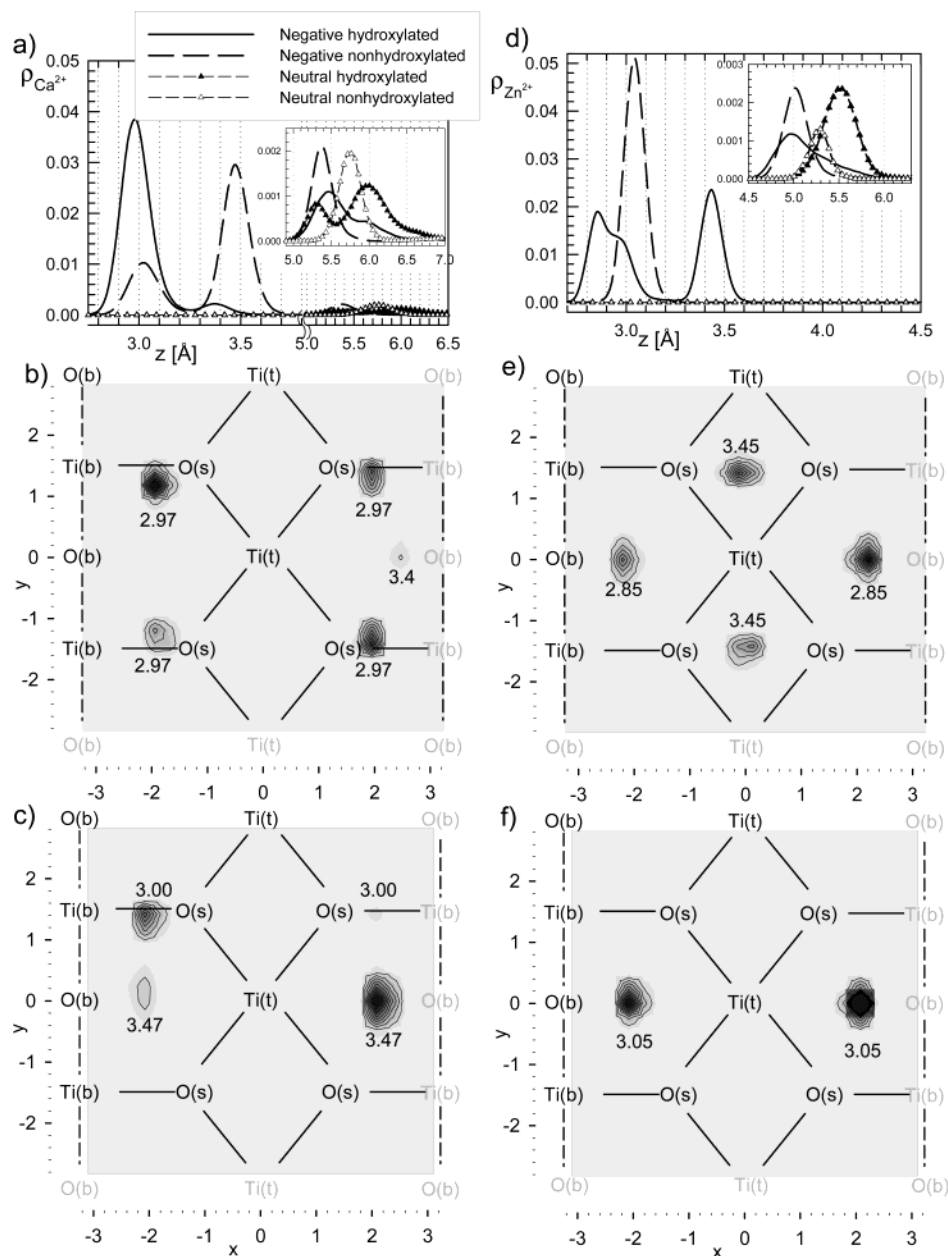


**Figure 5.** Same as Figure 4 but for  $\text{Ca}^{2+}$  ions (left column) and  $\text{Zn}^{2+}$  (right column). For zinc, the sites at 2.85 and 3.05 Å are bidentate between terminal oxygen and bridging oxygen, and the one at 3.45 Å is bidentate between two terminal oxygens.

consequently its small scattering factor) make it difficult to distinguish at low concentrations from the background water density profile. Attempts to detect  $\text{Br}^-$  adsorption, either as a coadsorbed species with  $\text{Sr}^{2+}$  at negatively charged surfaces or even on positively charged rutile (110) single crystal surfaces, by synchrotron XSW failed to indicate any ordering of this anion above the surface.<sup>18,23</sup>

At neutral surfaces, a very weak peak of the  $\text{Cl}^-$  density profile from MD simulation is located at about 5–5.5 Å above the nonhydroxylated surfaces and 6.5 Å for hydroxylated surfaces (Figure 6). Even though the interaction with coadsorbing cations evidently plays a significant role in determining this preferential separation of  $\text{Cl}^-$  from the surface (in addition to direct interactions with the surface and complex hydrogen structure), the location of these peaks varies by less than 0.3 Å for different cations. The peak density is about 4 times the homogeneous density of  $\text{Cl}^-$ , as opposed to factor of 20–50 for cation sorption, which demonstrates the low affinity of  $\text{Cl}^-$  toward the surface. For the neutral hydroxylated surface, an

additional small  $\text{Cl}^-$  peak at 4.3 Å results from direct interaction with hydrogens of surface hydroxyls. In all cases, the lateral distribution of  $\text{Cl}^-$  is flat, lacking any significant lateral ordering.

If the surface is positively charged, adsorption of  $\text{Cl}^-$  is expected to occur. To illustrate this phenomenon, we performed two simulations of positively charged hydroxylated and nonhydroxylated surfaces with  $\text{RbCl}$  solution, with 12  $\text{Rb}^+$  ions and 48  $\text{Cl}^-$  ions. The positive hydroxylated surface was prepared from the neutral hydroxylated surface by removal of  $1/4$  of the terminal hydroxyls; the positive nonhydroxylated surface was prepared from neutral nonhydroxylated surface by protonation of  $1/4$  of the bridging oxygens. In both cases the surface charge density was  $+0.208 \text{ C/m}^2$ . This is an extreme case, since powder titration studies indicate that such high positive surface charge densities would only occur in solutions with  $\text{pH} < 2$ .<sup>22</sup> The procedure described in ref 1 for determination of surface charges at a negatively charged surface was applied for determination of surface charges at a positively charged surface. The resulting axial density profile of  $\text{Cl}^-$  at a positively charged hydroxylated



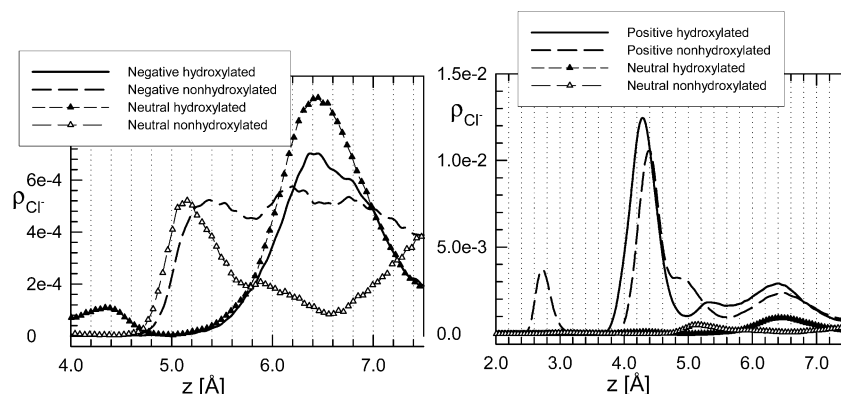


**Figure 6.** Axial density profiles of  $\text{Cl}^-$  at negative (left) and positive (right) surfaces with profiles for neutral surfaces given in both cases.

surface, shown in Figure 6, features the first broad peak with a maximum at 4.3 Å of  $\text{Cl}^-$  adsorbed at a tetradentate site where the interaction with hydrogens attached to the bridging and terminal oxygens is the determining factor. This peak covers only half the anions needed to compensate the surface charge, which results in increased density of  $\text{Cl}^-$  and water orientation up to about 10 Å from the surface plane. The axial density profile of  $\text{Cl}^-$  at a positively charged nonhydroxylated surface features the tetradentate peak as well, at 4.4 Å, but in addition a smaller peak at 2.7 Å is present, which covers partially desolvated  $\text{Cl}^-$  ions, which substitute chemisorbed water molecules above 5-fold coordinated terminal Ti.

#### 4. Discussion

It would be desirable to have a tool that would enable us to predict the existence of a particular type of adsorption site and its location, based on simple input, ideally without the need to run molecular simulations or conduct synchrotron X-ray studies. In cases where this predictions fails, the comparison between MD or X-ray results and simple geometric prediction informs us that more complex effects (e.g. change of the cation–oxygen bond lengths for surface oxygens, TO, and BO, relative to the bulk value) take place. To be able to better understand the influence of ion size on adsorption geometry, we investigate the performance of a simple geometric prediction of adsorption sites outlined as follows.

To investigate the variation of cation–O bond lengths for different O species, we determine the ion–oxygen pair correlation functions separately for oxygen of water molecules ( $\text{O}^{\text{H}_2\text{O}}$ ), unprotonated bridging oxygen ( $\text{O}^{\text{BO}}$ ), protonated bridging oxygen ( $\text{O}^{\text{BOH}}$ ), and terminal oxygen ( $\text{O}^{\text{TOH}}$ ). These correlation functions are shown in Figure 7. The comparison of the curves for hydroxylated and nonhydroxylated surfaces reflect the differences in the surface geometry; for example, the  $\text{Rb}^+ - \text{O}^{\text{TOH}}$  peak is twice as high for the hydroxylated surface, since in this case both oxygens above terminal Ti are terminal hydroxyls, while at the nonhydroxylated surface one of them belongs to an associated water molecule. Similarly, there are no protonated bridging oxygens on the nonhydroxylated surface, while on the negative hydroxylated surface  $3/4$  of the bridging oxygens are protonated. Nevertheless, the positions of the first peaks, summarized in Table 4, are rather similar regardless of the type of oxygen; the shorter separation of  $\text{Rb}^+$  from surface oxygens than that observed in bulk SPC/E water can be explained by the more negative charge (about  $-1e$ ) of the surface oxygens obtained from the ab initio calculations, compared to  $-0.8476e$  charge of oxygen in SPC/E water. When we attempt to quantitatively predict the possible adsorption sites, it is necessary to input the cation–O distance  $d_{\text{ion-O}}$  determined

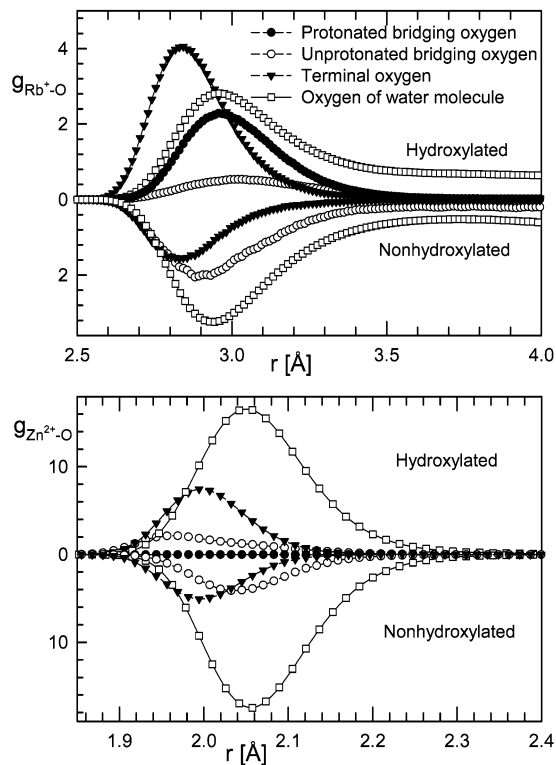


**Figure 7.**  $\text{Rb}^+ - \text{O}$  pair correlation functions (top) and  $\text{Zn}^{2+} - \text{O}$  pair correlation functions (bottom) for unprotonated bridging oxygen ( $\text{O}^{\text{BO}}$ ), protonated bridging oxygen ( $\text{O}^{\text{BOH}}$ ), terminal oxygen ( $\text{TO}$ ), and oxygen of water molecules ( $\text{O}^{\text{H}_2\text{O}}$ ). Note the absence of contribution from protonated bridging oxygen for  $\text{Zn}^{2+}$ , which indicates lack of tetradentate adsorption. Data for the negatively charged hydroxylated surface are shown in the upper half and those for the negatively charged nonhydroxylated surface are shown in the bottom half of the figure, as a mirror image plot.

from simulated pair correlation functions, integral equations, or previously published results.<sup>17,25</sup> We note that the peak of the ion–O pair correlation functions can be obtained from simulations or calculations of systems, which are easier to study than our simulations in a slab geometry, such as the homogeneous bulk ionic system.

Once the cation–O distance is determined, it is easy to predict possible adsorption sites based on two assumptions: (i) the adsorption site is primarily given by the position of the bridging oxygens and oxygens above the terminal Ti and (ii) these oxygens do not tilt significantly from their bulklike positions above the site bisecting two bridging Ti and the site above terminal Ti, respectively. The first assumption is well justified

**TABLE 4: Positions of First Peaks of Cation–Oxygen Pair Correlation Functions<sup>a,b</sup>**

ion	O <sup>BOH</sup>	O <sup>BO</sup>	TO	O <sup>H<sub>2</sub>O</sup>
Rb <sup>+</sup>	2.96	3.02	2.84	2.96
Rb <sup>+</sup>		2.88	2.83	2.94
Na <sup>+</sup>	2.56	2.58	2.40	2.47
Na <sup>+</sup>		2.41	2.40	2.47
Sr <sup>2+</sup>	2.83	2.69	2.58	2.64
Sr <sup>2+</sup>		2.61	2.56	2.64
Ca <sup>2+</sup>	2.63	2.53	2.40	2.47
Ca <sup>2+</sup>		2.41	2.39	2.45
Zn <sup>2+</sup>	3.48	1.97	1.99	2.06
Zn <sup>2+</sup>		2.03	1.99	2.06

<sup>a</sup> Protonated bridging oxygen (O<sup>BOH</sup>), unprotonated bridging oxygen (O<sup>BO</sup>), terminal oxygen (TO), and oxygen of water molecule (O<sup>H<sub>2</sub>O</sup>).

<sup>b</sup> The first row for each ion is for negative hydroxylated surface; the second row is for negative nonhydroxylated surface.

considering the termination of the (110) rutile surface with the Ti atoms lying deeper in the surface layer and BO and TO atoms exposed at the interface. In fact, it turns out that even the role of the in-plane surface oxygens O(s) is weak for adsorption of ions, due to spatial separation between these oxygens and the sorbing cations. The second assumption is well obeyed for bridging oxygens, which form two bonds to surface Ti. The terminal oxygens experience greater freedom and can tilt more from the vertical position above terminal Ti, but still the deviations are small, as shown in Figure 5 of ref 1. Assuming that the oxygens are localized in their ideal geometries, one can easily find both the height  $z$  and the  $x$  coordinate of tetradentate and bidentate sites, which satisfy conditions of all cation–O distances being equal to those derived from cation–O PCF. The resulting estimated geometries are summarized for all cations in Table 3. Note that this simple geometric consideration can only predict possible adsorption sites but gives no information on which of these sites is more frequently populated (if at all). It is the role of molecular simulations to consider all interactions involved and to show which adsorption sites are preferred and how much they differ from the idealized predicted sites.

For Rb<sup>+</sup>, the predicted height of the tetradentate site, 3.55 Å, is in excellent agreement with the MD observed height of 3.5–3.55 Å, as well as the prediction of the bidentate site, which, however, is observed in MD only at the negative nonhydroxylated surface and has not been identified experimentally.

For Na<sup>+</sup>, with a Na<sup>+</sup>–O distance of 2.47 Å, the estimated tetradentate site height of 2.70 Å is less than the height of 2.9 Å seen in MD simulations. The geometric prediction of the bidentate site height at 3.35 Å is in very good accord with the MD observed position at 3.42 Å for the negative nonhydroxylated surface.

From the Sr<sup>2+</sup>–O distance of 2.64 Å from Figure 1 and Table 1, the geometrically estimated heights of the tetradentate and bidentate sites are 3.04 and 3.59 Å. Similar to Na<sup>+</sup>, the geometric prediction slightly underestimates the actual MD heights, with a larger discrepancy for the tetradentate site. The same finding applies to Ca<sup>2+</sup>.

Using our geometric arguments, we find that Zn<sup>2+</sup> is too small to adsorb in the tetradentate site; the corresponding equations have no solution for  $d_{\text{ion-O}} = 2.06$  Å. The minimum ion–oxygen distance of any ion in a tetradentate site, in the plane formed by two bridging and two terminal oxygens, is 2.23 Å, which is significantly larger than the preferred Zn<sup>2+</sup>–O distance. Therefore, the tetradentate site is not favored by Zn<sup>2+</sup>, and this is confirmed by both the MD and X-ray results. The geo-

metrically predicted height of both bidentate sites, given in Table 3, is in excellent agreement with both sites observed by MD at negative hydroxylated surfaces. Since neither of the bidentate sites involves a protonated bridging oxygen, which participates only in adsorption at the tetradentate site, there is no peak of the Zn<sup>2+</sup>–O<sup>BOH</sup> pair correlation function around the location of the first peaks of other pair correlation functions.

The overall performance of the simple geometric prediction, based on average cation–oxygen distance only, is very good in all cases for both adsorption height  $z$  and position  $x$ , with quantitative agreement in many cases. This confirms that the ionic size is the major factor in determining the adsorption geometry of cations on negatively charged rutile (110) surfaces, coupled with the explicit atomic structure of the surface. It is of interest to note, in this respect, that XSW studies of Y<sup>3+</sup> adsorption on the rutile (110) surface<sup>18,19</sup> also indicate that this ion adsorbs exclusively at the tetradentate site. Since the experimental Y<sup>3+</sup>–O separation is 2.36 Å,<sup>17</sup> this finding is consistent with the criterion that the cation–O distance must be larger than 2.23 Å to allow tetradentate adsorption on (110) rutile surface. This further supports the notion that cation size is far more important than cation charge in determining the sorption site geometry. A future effort will include simulations covering the full range of alkali metal cations (Li<sup>+</sup>–Cs<sup>+</sup>) for which SPC/E water–ion interaction parameters are available from the same self-consistent source,<sup>10</sup> with the bare radius of Li<sup>+</sup> (0.69 Å) being smaller than that of Zn<sup>2+</sup>, and the radius of Cs<sup>+</sup> (1.7 Å) being considerably larger than that of any of the cations investigated thus far.

## 5. Conclusions

We have performed a series of molecular dynamics simulations of aqueous electrolyte solutions in contact with rutile (110) surfaces to determine the effect of surface charge and hydroxylation on adsorption of Rb<sup>+</sup>, Na<sup>+</sup>, Sr<sup>2+</sup>, Zn<sup>2+</sup>, and Ca<sup>2+</sup> ions at the metal oxide–aqueous solution interface. We have used an atomically detailed model of the rutile (110) surface parametrized with ab initio calculations and assumed that ion–surface oxygen interaction potentials are the same as for SPC/E water molecule interactions with ions. Because of the relatively low p*H*<sub>pzc</sub> of rutile (~5.4 at 25 °C), and the observation that cations interact much more strongly than anions with rutile surfaces, we concentrated on simulations of negatively charged rutile surfaces. For comparison, we have studied the structure of the interface at neutral surfaces as well. This comparison clearly shows that the surface charge is the dominant factor in driving ion adsorption, as expected. At the same time, the resulting cation adsorption geometries are found to be relatively insensitive to the magnitude of the specific surface charge density, which translates into the number of charged surface groups and determines only the concentration of adsorbed ions. MD simulations show that the adsorption structures at surface charge densities –0.208 and –0.104 C/m<sup>2</sup> differ by less than 0.05 Å; that is, the results presented here for one surface charge density are representative for an important range of negative surface charge densities occurring in real rutile. Even at hydroxylated surfaces with no net surface charge density, MD simulations show that the more weakly hydrated cations still adsorb at the same sites, although at much lower densities, and at heights somewhat higher than for the negatively charged surfaces, whereas ions that are strongly hydrated (Sr<sup>2+</sup>, Zn<sup>2+</sup>) show very weak interaction with neutral hydroxylated surfaces. No cations investigated are significantly attracted to neutral nonhydroxylated surfaces.

A central issue in this study was the determination of the nature of the rutile–water interface hydration structure; that is, which of the two competing surface configuration models (hydroxylated or nonhydroxylated) provides a better description of ion adsorption behavior for charged rutile surfaces. For the *nonhydroxylated* surface, we found that all ions except  $\text{Zn}^{2+}$  adsorb preferentially at a tetradentate site on negative surfaces, involving two terminal and two bridging oxygens. As the ion size decreases, the bidentate site between terminal and bridging oxygens becomes competitive on negatively charged nonhydroxylated surfaces, at least in the MD simulations. The bidentate site appears as marginal for  $\text{Rb}^+$  but dominant for  $\text{Na}^+$ . The same trend is observed for  $\text{Sr}^{2+}$  and the smaller  $\text{Ca}^{2+}$  ion, though the bidentate site is predicted by MD to be dominant for both of these divalent cations on the negative, nonhydroxylated surface.

In contrast, simulations for the *negative hydroxylated* surface show that the tetradentate site is the dominant adsorption site for all ions ( $\text{Na}^+$ ,  $\text{Rb}^+$ ,  $\text{Ca}^{2+}$ , and  $\text{Sr}^{2+}$ ) except  $\text{Zn}^{2+}$ . Significantly, in situ X-ray CTR and XSW studies of the sorption of  $\text{Rb}^+$  and  $\text{Sr}^{2+}$  on negatively charged rutile (110) single crystal surfaces in aqueous solutions at high pH show only one significant adsorption site for both of these ions, and this corresponds to the MD-predicted height and lateral positions of these ions in the tetradentate site.<sup>18,19</sup> The adsorption of  $\text{Zn}^{2+}$ , the smallest of all the ions studied, is completely different from the other ions studied. Zinc is too small to adsorb at the tetradentate site and instead adsorbs in a bidentate site between terminal and bridging oxygens for both negative surfaces; at negative hydroxylated surfaces, there is a second bidentate adsorption site between two terminal oxygens. Once again, synchrotron XSW studies of  $\text{Zn}^{2+}$  on rutile (110) single-crystal surfaces agree better with the hydroxylated surface configuration, since two distinct sorption sites are observed.<sup>18,19</sup> Thus, the comparison of MD- and X-ray-based observations of ion adsorption sites suggests that the charged hydroxylated surface model, rather than the nonhydroxylated model, provides the closest approximation of the real rutile–water interface. Although there is general agreement concerning adsorption sites for all ions, and the precise ion positions for  $\text{Rb}^+$  and  $\text{Sr}^{2+}$ , there remains a significant discrepancy between the X-ray and MD results regarding the heights of  $\text{Zn}^{2+}$  ions above the Ti–O surface for these two sites. Single-crystal grazing incidence extended X-ray absorption fine structure (EXAFS) studies of  $\text{Co}^{2+}$  sorption on rutile (110) surfaces<sup>26</sup> also indicated sorption at either one or both of the projected Ti sites (corresponding to monodentate adsorption above the BO and/or bidentate adsorption between TO sites) but do not directly provide information concerning the height of the ion with respect to the surface plane. These observations correspond fairly well with those observed for  $\text{Zn}^{2+}$  on the negative hydroxylated surface, which is to be expected, since aqueous  $\text{Co}^{2+}$  and  $\text{Zn}^{2+}$  have nearly identical ionic radii.

X-ray CTR studies of  $\text{Na}^+$ ,  $\text{K}^+$ , and  $\text{Ca}^{2+}$  adsorbed at rutile surfaces may provide further tests of the hydroxylated surface model for rutile in liquid water, but since the scattering factors of these ions are within a factor of 2 of that of a water molecule, the ion location for these ions is more difficult to uniquely constrain than was the case for  $\text{Rb}^+$ , which has a scattering factor that is a factor of  $\sim 4$  larger than that of a water molecule. Since such measurements rely upon observing changes in the total interfacial electron density, which will necessarily be substantially smaller with such low- $Z$  cations, we would expect increased uncertainties in determination of the ion location.

Since we use a nondissociative model of water in our simulations, we cannot observe the hydroxylation as a dynamic feature, but we infer from this study that the rutile surface in contact with aqueous solutions is substantially hydroxylated. So far the available ab initio results indicate that the surface is rather nonhydroxylated at up to 1 monolayer coverage of water molecules and partial hydroxylation occurs at higher coverages.<sup>27–29</sup> However, no such calculations have been performed involving a sufficient number of water molecules to mimic more realistically the interface of rutile with bulk liquid water at densities approaching 1 g/cm<sup>3</sup>.

Our results reveal that ion size, as quantified by the position of the first peak of ion–oxygen pair correlation function, is a key parameter in determining the ion adsorption geometry. We have tested a simple geometric rule to predict the positions of adsorption sites on rutile (110), based on the size of ions. This estimate proves to be rather good, especially for the bidentate sites, and can also determine whether the formation of a tetradentate site is possible for a given ionic size. Though the relative population of possible adsorption sites needs to be determined from MD simulations coupled with X-ray and other types of surface imaging techniques with subangstrom resolution, our conclusions suggest that analysis of MD results of adsorption of ions and their interpretation makes a significant step toward qualitative and quantitative predictions of interfacial phenomena. It has recently been demonstrated<sup>16</sup> that application of surface complexation models (SCMs) to powder–pH titration studies of  $\text{Ca}^{2+}$  adsorption on rutile surfaces cannot produce unambiguous interpretations of the double layer structure without such atomistic detail, ideally provided by a combination of subangstrom imaging studies and ab initio-constrained MD simulations.

Heretofore, it has been frequently postulated that so-called indifferent electrolyte ions (typically 1:1 salts of the alkali metals) do not interact specifically with metal oxide surfaces.<sup>30,31</sup> However, this study and our coordinated X-ray experiments<sup>18</sup> definitively demonstrate for the first time that all cations studied, including  $\text{Rb}^+$ ,  $\text{Na}^+$ , and the weakly sorbing divalent cation  $\text{Sr}^{2+}$ , form inner-sphere complexes with the surface oxygens exposed at the rutile (110) surface in aqueous solutions. Additionally, though these ions may also be concentrated to some extent in the diffuse portion of the electrical double layer, our MD simulation results suggest that beyond the surface layer of specific adsorption, such ions exhibit only weak ordering perpendicular to the surface and little or no lateral ordering, and no definitive indication of such ions has been found in the X-ray results to date. The observation of surface contact of sorbing cations on rutile (110) surfaces is consistent with the recent hypothesis<sup>32</sup> that metal oxides with high bulk dielectric constants, like rutile, magnetite ( $\text{Fe}_3\text{O}_4$ ), etc., should exhibit inner-sphere binding of cations, with the distance of approach of sorbed cations to the surface correlating with their bare ionic radii. An additional prediction of this hypothesis is that low bulk dielectric solids, such as quartz ( $\alpha\text{-SiO}_2$ ) and corundum ( $\alpha\text{-Al}_2\text{O}_3$ ), should be characterized by outer-sphere binding of most cations, with the distance of closest approach correlated with the hydrated radii of the ions in solution. Further tests of this interesting hypothesis should lead to a greatly enhanced ability to predict and understand the macroscopic manifestations of oxide–water interfacial phenomena.

Our MD simulations at 448 K and 0.9 g/cm<sup>3</sup>, corresponding to liquid water near the liquid–vapor saturation pressure, show no significant changes in water structure<sup>1</sup> or the locations and populations of specific ion adsorption sites, relative to ambient



conditions. If this can be verified experimentally, it will provide an important constraint on site complexation models applied to high-temperature pH titration studies of rutile powder suspensions (e.g., refs 16 and 33), which indicate that Stern layer capacitances of multivalent cations increase significantly with increasing temperature. The capacitance is a function of the distance of separation of the Stern plane from the plane of surface charge and of the dielectric constant of the medium in the Stern layer; the latter thus remains as a primary factor in determining the temperature dependence of the Stern layer capacitance.

**Acknowledgment.** We thank the Division of Chemical Sciences, Geosciences, and Biosciences, Office of Basic Energy Sciences, U.S. Department of Energy, for support of this research under the project Nanoscale Complexity at the Oxide–Water Interface (ERKCC41) and the Center for Computational Sciences at Oak Ridge National Laboratory and National Energy Research Supercomputing Center (NERSC) at Lawrence Berkeley Laboratory for computer time. M.P. acknowledges support by the Grant Agency of the Czech Republic (Grants 203/03/P083 and 203/02/0805).

## References and Notes

- Předota, M.; Bandura, A. V.; Cummings, P. T.; Kubicki, J. D.; Wesolowski, D. J.; Chialvo, A. A.; Machesky, M. L. *J. Phys. Chem. B* **2004**, *108*, 12049–12060 (preceding paper in this issue).
- Bedzyk, M. J.; Cheng, L. X-ray Standing Wave Studies of Minerals and Mineral Surfaces: Principles and Applications. In *Applications of Synchrotron Radiation in Low-Temperature Geochemistry and Environmental Science*; Fenter, P., Rivers, M., Sturchio, N. C., Sutton, S., Eds.; Reviews in Mineralogy and Geochemistry, Vol. 49; Geochemical Society: Washington, D.C., 2002; pp 221–226.
- Zegenhagen, J. *Surf. Sci. Rep.* **1993**, *18*, 199.
- Robinson, I. K.; Tweet, D. J. *Rep. Prog. Phys.* **1992**, *55*, 599.
- Fenter, P. X-ray Reflectivity as a Probe of Mineral–Water Interfaces: A User Guide. In *Applications of Synchrotron Radiation in Low-Temperature Geochemistry and Environmental Science*; Fenter, P., Rivers, M., Sturchio, N. C., Sutton, S., Eds.; Reviews in Mineralogy and Geochemistry, Vol. 49; Geochemical Society: Washington, D.C., 2002; pp 149–220.
- Bandura, A. V.; Kubicki, J. D. *J. Phys. Chem. B* **2003**, *107*, 11072.
- Bandura, A. V.; Sykes, D. G.; Kubicki, J. D. Adsorption of water on the TiO<sub>2</sub> (rutile) [110] surface: A DFT study. *J. Phys. Chem. B* **2004**, *108*, 7844.
- Berendsen, H. J. C.; Grigera, J. R.; Straatsma, T. P. *J. Phys. Chem.* **1987**, *91*, 6269.
- Palmer, B. J.; Pfund, D. M.; Fulton, J. L. *J. Phys. Chem.* **1996**, *100*, 13393.
- Lee, S. H.; Rasaiah, J. C. *J. Phys. Chem.* **1996**, *100*, 1420.
- Guissani, Y.; Guillot, B. *J. Chem. Phys.* **1993**, *98*, 8221.
- Chialvo, A. A.; Cummings, P. T.; Simonson, J. M.; Mesmer, R. E.; Cochran, H. D. *Ind. Eng. Chem. Res.* **1998**, *37*, 3021.
- Chialvo, A. A.; Cummings, P. T. In *Advances in Chemical Physics*; Prigogine, I., Rice, S. A., Eds.; John Wiley and Sons: New York, 1999; Vol. 109, pp 115–204.
- Hansen, J. P.; McDonald, I. R. *Theory of Simple Liquids*; Academic Press: New York, 1986.
- Löffler, G.; Schreiber, H.; Steinhäuser, O. *J. Chem. Phys.* **1997**, *107*, 3135.
- Ridley, M. K.; Machesky, M. L.; Wesolowski, D. J.; Palmer, D. A. *Geochim. Cosmochim. Acta* **2004**, *68*, 239.
- Marcus, Y. *Chem. Rev.* **1988**, *88*, 1475.
- Zhang, Z.; Fenter, P.; Cheng, L.; Sturchio, N. C.; Bedzyk, M. J.; Předota, M.; Bandura, A.; Kubicki, J.; Lvov, S. N.; Cummings, P. T.; Chialvo, A. A.; Ridley, M. K.; Bénézeth, P.; Anovitz, L.; Palmer, D. A.; Machesky, M. L.; Wesolowski, D. J. *Langmuir* **2003**, *20*, 4954.
- Zhang, Z.; Fenter, P.; Cheng, L.; Sturchio, N. C.; Bedzyk, M. J.; Machesky, M. L.; Wesolowski, D. J. *Surf. Sci. Lett.* **2004**, *554*, L95.
- Fenter, P.; Cheng, L.; Rihs, S.; Machesky, M.; Bedzyk, M. J.; Sturchio, N. C. *J. Colloid Interface Sci.* **2000**, *225*, 154.
- Marcus, Y. *Ion Properties*; Marcel Dekker: New York, 1997; p 259.
- Machesky, M. L.; Palmer, D. A.; Wesolowski, D. J.; Hayashi, K. I. *J. Colloid Interface Sci.* **1998**, *200*, 298.
- Zhang, Z.; Fenter, P.; Cheng, L.; Sturchio, N. C.; Bedzyk, M. J.; Machesky, M. L.; Wesolowski, D. J. Manuscript in preparation.
- Criscenti, L. J.; Sverjensky, D. A. *Am. J. Sci.* **1999**, *299*, 828.
- (a) Shannon, R. D.; Prewitt, C. T. *Acta Crystallogr. B* **1969**, *25*, 925. (b) Shannon, R. D.; Prewitt, C. T. *Acta Crystallogr. B* **1970**, *26*, 1046.
- Towle, N.; Brown, G. E., Jr.; Parks, G. A. *J. Colloid Interface Sci.* **1999**, *217*, 299.
- Lindan, P. J. D.; Harrison, N. M. *Phys. Rev. Lett.* **1998**, *80*, 762.
- Zhang, C.; Lindan, P. J. D. *J. Chem. Phys.* **2003**, *118*, 4620.
- Langel, W. *Surf. Sci.* **2002**, *496*, 141.
- Dzombak, D. A.; Morel, F. M. M. *Surface Complexation Modeling—Hydrous Ferric Oxide*; Wiley-Interscience: New York, 1990; p 393.
- Lyklema, J. *Pure Appl. Chem.* **1991**, *63*, 895.
- Sverjensky, D. A. *Geochim. Cosmochim. Acta* **2001**, *65*, 3643.
- Ridley, M. K.; Machesky, M. L.; Wesolowski, D. J.; Palmer, D. A. *Geochim. Cosmochim. Acta* **1999**, *63*, 3087.